HHS Public Access

Author manuscript

Nat Struct Mol Biol. Author manuscript; available in PMC 2019 June 30.

Published in final edited form as:

Nat Struct Mol Biol. 2019 January ; 26(1): 40–49. doi:10.1038/s41594-018-0168-8.

Structures of TRPV2 in distinct conformations provide insight into role of the pore turret

Timothy L. Dosey[#1], **Zhao Wang**[#1], **Guizhen Fan**[2], **Zhixian Zhang**[1], **Irina I. Serysheva**[2], **Wah Chiu**[1,3,*], and **Theodore G. Wensel**[1,*]

[1]Verna and Marrs Mclean Department of Biochemistry and Molecular Biology, Baylor College of Medicine, Houston, TX 77030, USA

[2]Department of Biochemistry and Molecular Biology, Structural Biology Imaging Center, McGovern Medical School at the University of Texas Health Science Center at Houston, Houston, TX 77030, USA

[3]Departments of Bioengineering and of Microbiology and Immunology, Stanford University, Stanford, CA 94305-5447

[#] These authors contributed equally to this work.

Abstract

Cation channels of the TRP family serve important physiological roles by opening in response to diverse intra-and extra-cellular stimuli which regulate their lower or upper gates. Despite extensive studies, the mechanism coupling these gates has remained obscure. Previous structures have failed to resolve extracellular loops, known in the TRPV subfamily as “pore turrets,” which are proximal to the upper gates. We establish the importance of the pore turret through activity assays and by solving structures of rat TRPV2 both with and without an intact turret at resolutions of 4.0 Å and 3.6 Å respectively. These structures resolve the full-length pore turret and reveal fully open and partially open states of TRPV2, both with unoccupied vanilloid pockets. Our results suggest a mechanism by which physiological signals, such as lipid binding, can regulate the lower gate and couple to the upper gate through a pore turret-facilitated mechanism.

Introduction

Transient Receptor Potential channels are conserved throughout eukaryotes and respond to extra- and intracellular chemical, mechanical, and temperature stimuli [1,2]. In mammals,

[*]Correspondence: twensel@bcm.edu (T.G.W.), wahc@stanford.edu (W.C.).
Lead Contact: Theodore G. Wensel, twensel@bcm.edu

Author contributions:

T.L.D. designed the project, designed and performed all biochemistry and molecular biology experiments, processed cryo-EM data, constructed and optimized the molecular models, prepared figures and animations, and wrote the manuscript. Z.W. and G.F. collected cryo-E.M. data, and Z.W. reconstructed, refined, and validated the maps. Z.Z. collected and processed preliminary cryo-EM data to optimize cryo-specimen preparation for high resolution imaging. T.G.W, W.C. and I.I.S. supervised personnel, provided laboratory resources and facilities, participated in structure interpretations and edited the manuscript.

Competing interests

The authors declare no competing interests.

there are 6 subfamilies each with distinct domain structures, expression profiles, and activation modalities [1,3]. Mutations in TRP channels result in diverse human diseases including spontaneous pain syndrome, night blindness, and polycystic kidney diseases [4–7]. Because of their wide-ranging physiological roles, many are promising drug targets [8].

Clinical trials studying members of the polymodal TRPV subfamily have been conducted targeting the TRPV1 channel for pain and TRPV4 to promote heart failure recovery. Although promising results have been produced, TRPV-targeted therapies are not yet widely available in the clinic and many lead compounds targeting TRPV1 have failed because of the undesirable side effect of hyperthermia [9,10]. There is hope that side-effects can be overcome by designing modality specific drugs but our understanding of the mechanisms regulating activity in these channels is incomplete [11,12]. Recently, near-atomic resolution structures for TRPV1, TRPV2, and TRPV6 have revealed that in addition to the lower gate found in related voltage-gated potassium channels, there is an upper gate corresponding to the selectivity filter region of the K^+ channels [13–18]. The mechanisms regulating the conformations of these two gates and how they are coupled to allow cation permeation in response to physiological stimuli have remained elusive.

All high-resolution structures for thermo-sensitive TRP channels published to date have either lacked or have failed to resolve the long extracellular loops proximal to their upper gates [13,15–17,19,20]. This loop immediately precedes the pore helix and selectivity filter in the heat-sensitive TRPV1, TRPV2, and TRPV4 channels, and is called the pore turret[13–17]. The constructs used for the high resolution TRPV1 and TRPV2 structures contained large deletions in this loop to enhance stability and facilitate structure determination. The structures lacking potent exogenous agonists have all adopted closed conformations, and in all of them except for 6BWM[20], their vanilloid binding sites are occupied either by an exogenous ligand or by density attributed to lipid, leaving the endogenous mechanism of opening still unclear. While one published TRPV2 structure (PDB: 5HI9)[16] contained the pore turret, its resolution was too low either to resolve the pore turret or to reveal the functional state. Nevertheless, the model of this structure also appears to be in a closed state (Supplementary Fig. 1a). A long extracellular loop is also present in the cold-sensing TRPM8[19] channel and immediately follows the pore helix and selectivity filter; however, it again was not resolved in the recently published cryo-EM structure. Therefore, despite the published structures, the contribution these extracellular loops make to the structure and function of temperature-sensitive TRP channels has remained unclear.

The extracellular pore turret loop and its role in TRPV channel function have remained enigmatic and have been the subject of some controversy[15,16,21–27]. Electrophysiological studies performed by different groups have produced different conclusions concerning its involvement in the modalities of activation by heat, ligands, and protons. Substitutions of a poly-glycine chain in the TRPV1 pore turret position resulted in ablated temperature sensing without affecting capsaicin activation, whereas pore turret deletions (~11-20 amino acids) did not affect temperature sensing and had a mild effect on capsaicin and proton activation[21,22]; a glutamate residue within the TRPV1 pore turret was reported to be important for acid sensing[26]. In addition, large TRPV1 turret deletions (minimal TRPV1 function construct) did produce an approximately 3-fold reduction in potency for DkTx,

which binds proximally to the pore turret[15], reduced activation by DkTx relative to capsaicin, and increased potency of inhibition by external Na^+ [25]. Two point mutations within TRPV1 were found to increase permeability to a large organic cation, and two others were found to reduce it[28]. One group found that a 26 residue deletion within the pore turret of rat TRPV2 nearly abolished responses to 2-APB in cell-based assays[16], while another found that the corresponding deletion within rabbit TRPV2 had little effect[17], Suggesting some effects of pore turret deletions in TRPV2 may be species specific. It is unclear whether the pore turret is necessary for TRPV channel function, but it does appear to play a modulating role in channel activity, perhaps in a modality specific way, and the structural basis for such a role is unknown.

Here we present two structures determined by single-particle cryo-EM for rat TRPV2 with a full length pore turret and with a pore turret deletion at resolutions of 4 Å and 3.6 Å, respectively. These structures not only resolve the pore turret for the first time, demonstrating that it has a well-defined structure, but also demonstrate that it is necessary for the S6 helix, pore loop, and selectivity filter to adopt an open conformation. In addition to the structures, we have confirmed the activity differences among different TRPV1, TRPV2 and TRPV4 constructs with long or short pore turrets, and observed inhibitory effects of phosphatidylinositol 4, 5 bisphosphate (PIP_2) on TRPV2 with an intact pore turret.

Results:

Pore turret manipulations alter TRPV channel activity

The pore turret sequence and length are poorly conserved across members of the TRPV subfamily, but the length is conserved among TRPV orthologues. TRPV1, TRPV2, and TRPV4 have relatively long pore turrets whereas TRPV3, and the more distantly related TRPV5 and TRPV6 channels have naturally short pore turrets (Fig. 1a). This extracellular loop forms the linker between the pore helix and the S5 segments which have been demonstrated to be components of the upper and lower gates respectively, so the suggestion that it has little functional importance seems surprising [13–15,17,18].

Although TRPV channel activity is routinely measured by voltage-clamp recordings at high positive potentials of around +60 to +100 mV [14,15,21–23,27], we wanted to test whether there are detectable changes in TRPV channel activity at physiological potentials in response to alterations in the pore turret sequence and length. Therefore, we used a cell-based Ca^{2+}-flux assay in HEK-293 cells to measure both WT and mutant channel dose responses to agonists, the details of which can be found in the methods section. Because the commonly used TRPV2 agonist, 2-APB, has low potency and specificity, and may not act on TRPV2 directly, we included TRPV2 variants bearing four point mutations previously shown to confer sensitivity to resiniferatoxin (RTX) [29,30]. We found that TRPV1, TRPV2, RTX-sensitive TRPV2, and TRPV4 all had significant decreases in agonist sensitivity amounting to a shift of ~10 fold in their EC_{50} values when their pore turrets were shortened to 8 residues (Fig. 1b-e).

The fully closed map previously reported for unliganded TRPV2[17] has unassignable density in the vanilloid pocket, and in the TRPV1-nanodisc structures (PDB:5IRZ)[13], a

phosphatidylinositol in this pocket could be modeled into the higher resolution map, raising the question of whether phosphoinositides or other lipids (as the identity of the bound lipid is uncertain) binding there may modulate activity. It has been reported that phosphoinositides inhibit the TRPV1[31] and TRPV3[32], but there have also been reports of activation of both TRPV2[33] and TRPV1[34] by PI(4,5)P_2 (PIP_2). It has been suggested that the sign of the effect depends on which side of the membrane contains the phosphoinositide[35] and that PIP_2 can have both positive and negative modulatory affects depending on conditions[36]. To determine effects of PIP_2 on TRPV2, we used both cell-based and liposome-based fluorescence activity assays to manipulate the PIP_2 levels in the inner leaflet of the plasma membrane or in the defined phospholipid bilayer (Fig. 1f,g). In the cell-based assay, we co-transfected cells with constructs expressing the WT TRPV2 channel, a plasma membrane anchored FRB domain, and a FKBP-fused PIP_2 phosphatase. With this system, we induced a rapid reduction in plasma membrane PIP_2 levels with the addition of rapamycin (rap) [37], and observed potentiated TRPV2 activity in response to 2-APB as compared to responses when PIP_2 remained at basal levels (Fig. 1f). Next, we tested for a PIP_2 inhibitory effect on TRPV2 in defined conditions using liposomes containing calcium-sensitive dye and reconstituted TRPV2. This assay reveals that WT TRPV2 is active in these conditions, as calcium freely enters liposomes containing TRPV2, but not those without the channel. However, when PIP_2 is added to the liposomes in a physiological 1:100 molar ratio to the bulk lipids, the TRPV2 activity is nearly abolished, implying a direct inhibitory effect of PIP_2 on TRPV2 (Fig. 1g). As noted above, effects of PIP_2 on TRPV channels may depend on which side of the membrane contains them, which is difficult to control in this sort of assay; it is also conceivable that the presence of 1% PIP_2 somehow influenced the efficiency of channel incorporation in a functional state into the bilayer. In the cell-based assay, it is clear that the change in lipid composition occurs at the cytoplasmic face, but it is conceivable that the product of the action of the phosphatase on PIP_2, PI(4)P, which has been reported to enhance TRPV1 activity under some conditions[34] may contribute to the observed effects. However, experiments using a very similar approach to PIP_2 depletion found that the levels of PI(4)P generated were not sufficient for TRPV1 activation[38]. Taken together these experiments are consistent with a scenario in which the activity of a constitutively active, or partially active, apo-TRPV2 with a full-length pore turret can be modulated by phosphoinositides or other lipids through binding at the vanilloid pocket or elsewhere; modulation by additional intracellular binding partners not assessed here is also likely.

To gain further insights into the possible roles of the pore turret and lipids in TRPV2 function and structure, we prepared constructs with and without a full-length pore turret (Fig. 2) without addition of any lipids during purification (in contrast to previous cryo-EM studies), in order to determine their structures by cryo-EM and single particle analysis.

Cryo-EM structures of TRPV2 variants

To enhance the likelihood of resolving a flexible loop like the pore turret within a TRPV channel, we selected TRPV2 for cryo-EM analysis because of the presence of 5 prolines in its turret sequence (P565, P568, P579, P587, P589). The low conformational freedom of these prolines [39] potentially stabilize the TRPV2 pore turret rendering it more suitable for

high-resolution structure determination than those of TRPV1 and TRPV4 whose turrets are similar in length but possibly less constrained. Thus, we created constructs for both WT rTRPV2 and rTRPV2 with a pore turret deletion (Δ564-589) for heterologous expression in *S. Cerevisiae* (Fig. 2a, 2b). While optimizing these constructs for expression and structural determination we removed the N- and C-termini, which are predicted to be disordered, but these deletions drastically reduced protein expression. However, we were able to rescue expression by adding the first 32 amino acids from the N-terminus of the endogenous yeast TRP channel, YVC1 to the TRPV2 N-terminus (Supplementary Fig. 2). This sequence was also able to enhance TRPV4 expression (Supplementary Fig. 2a, b). Activities for the constructs which were ultimately used for structure determination were then tested and their functions found to be similar to their less-modified TRPV2 counterparts without the truncated N- and C-termini (Supplementary Fig. 2f). To be clear and consistent, both constructs we used for our structural investigation have the same N- and C- terminal modifications and we designate the construct with the full-length pore turret as “WT” and the construct with the shortened pore turret as “Mutant”.

The details for the purification of the TRPV2 variants can be found in the methods section along with the information about grid preparation, cryo-EM data collection, and data processing. TRPV2 proteins purified using maltose neopentyl glycol (MNG) detergent for solubilization appeared by size exclusion chromatography and cryo-EM to be stable and monodisperse (Supplementary Figs. 2e, and 3). The final maps of TRPV2 and its variant were reconstructed to 4.0 and 3.6 Å resolution (Table 1 and Supplementary Fig. 4). The architecture and overall dimensions of the tetrameric TRP channel three-dimensional density maps are consistent with previously published structures by other groups (Fig. 2c and Supplementary Video 1) [13–18]. Due to the flexibility associated with particular domains, resolution and resolvability of structural features are different in various parts of the map (Supplementary Fig. 4a and 4d). The ankyrin repeat domain and transmembrane helices are well resolved in the maps with many side chains visible (Supplementary Fig. 4c, f). Coverage of the density differed slightly at the N-terminus resulting in ~10 Å difference in the width of the maps (Fig. 2c and d).

The biggest difference between the two maps occurs at the pore turret loop located on the extracellular side of the channel. It is clearly resolved in our WT TRPV2 map and as expected, there is a lack of density in the respective location on the mutant map (Fig. 2c, d and Supplementary Video 1).

Extracellular pore turret

The pore turret is defined as the extracellular loop region (S559-S592) connecting the S5 helix to the pore helix (I593-I605). Immediately following the pore helix is the selectivity filter (G606-E609) and pore loop (L610-F618), which are the other two components of the upper gate. Here we clearly resolve the pore turret to ~ 4 Å resolution (Supplementary Fig. 4a), and by adjusting the threshold of the density map, the path of the backbone can readily be traced and modeled within the experimental density (Fig. 2e, Fig. 3, Supplementary Fig. 5, and Supplementary Video 2). Multiple structure prediction programs were run for this loop’s sequence and all of them predicted a very low probability for either a β-sheet or α-

helix, further justifying our interpretation of this structure as a loop. Our map and model reveal that the pore turret forms a planar structure parallel to the plasma membrane and perpendicular to the cation conduction pathway of the channel (Fig. 3b and Supplementary Video 2). The backbone appears to fill the extracellular planar space between the adjacent subunits of the tetramer just above the plasma membrane. It comes close to the extracellular ends of S2β and S3α (Fig. 3a and Supplementary Video 2); however, direct interactions cannot be confidently assigned because of the flexibility of this region (see atomic displacement parameter map in (Supplementary Fig. 6). The pore turret contains turns at positions where density is visible for the first three of five proline residues which are thus reliably modeled; these proline-induced turns help maintain the planar conformation of the turret loop.

Specifically P568, which is one of the few residues conserved within this loop throughout mammals, comes closest to S2β of the adjacent subunit and produces a sharp turn in the pore turret (Fig. 3a and Supplementary Video 2). The distance between the C-terminal end of the S5 helix and the N-terminal end of the pore helix is ~7 Å; thus the 8 residue pore turrets would have sufficient length to connect these two helices, suggesting that the reduced flexibility of this area is not the primary reason for the reduction in channel activity observed in the deletion mutants.

Cation conduction pathway

By using the HOLE [40] program we calculated the Van der Waals radii of the conduction pathway for both the WT and mutant TRPV2 structures revealing that WT TRPV2 has wide openings at the upper and lower constrictions whereas the mutant, although also having an open lower gate, has a pore which appears more occluded (Fig. 4 and Supplementary Video 3). In the WT TRPV2 structure, the region of the selectivity filter facing the pore has relatively weak density and high atomic displacement parameters (Supplementary Fig. 4), consistent with a dynamic structure for this pore-lining motif, which forms the upper gate. Consequently, the positions of the atoms cannot be assigned unambiguously; however, density for bulky side chains such as E609 and M607 is seen clearly in the map, allowing a model with good geometry to be built. In the conductive WT structure, the best fitting model for this region places the E609 side chain and the backbone carbonyl of M607 pointing towards the center of the conduction pathway at the upper gate, which would facilitate cation binding and conduction (Fig. 4b, 4c and Supplementary Fig. 1c), and the hydrophobic side chain of M607 pointing away. This arrangement is similar to those observed in the open TRPV1 structures induced by toxins [13,14]. In contrast, the mutant TRPV2 upper gate appears constricted and the well resolved hydrophobic side chain of M607 points inwards toward the conduction pathway forming a hydrophobic ring and thereby inhibiting cation conduction (Fig. 4e, 4f, and Supplementary Fig. 1c and 1d).

Compared to the pores of the previously reported unliganded TRPV2 structures, which both appear fully closed (Supplementary Fig. 1a and 1b), the WT structure reported here appears fully open while the Mutant appears too occluded for cation conduction (Fig. 4c and 4f). Interestingly, the partially open state of the TRPV2 mutant is similar to what was observed in the capsaicin-bound TRPV1 structures (PDB:3J5R), which also had a partially open lower

gate while maintaining a fully closed upper gate. Both the TRPV1 (PDB:5IRZ) and our TRPV2 mutant constructs share homologous deletions in their pore turrets which could be why both fail to couple the opening of the upper gate with their partially open lower gates, and also why they show reduced agonist sensitivity in our activity assays(Fig. 1b,c,d) [13,14]. The Cα RMSD deviations in the selectivity filter and proximal pore loop between the WT open state and the nonconductive states are 3.34 Å (mutant structure) and 4.96 Å (previously published fully closed structure PDB:5AN8)[17] (Table 2).

Structural analysis of the voltage sensing-like domain and ankyrin repeats.

Although TRPVs are somewhat voltage sensitive[41], they lack the positively charged residues voltage-senstive cation channels have in the S4 helix of the voltage sensitive bundle (S1-S4). Therefore, the S1-S4 transmembrane domains of TRPVs is a voltage sensitive-like domain (VSLD) and has been thought to contribute little to channel activity. Supporting this idea are the previously published open and closed structures of TRPV1 which show very little movement in the VSLD. However, aligning the models of our fully open WT structure to the fully closed structure (PDB:5an8) reveals a prominent shift in the S3 helix towards S5 and the vanilloid pocket (Fig. 5a, b) with a Cα RMSD of 3.12 Å (Table 2). Furthermore, the position of the Y471 side chain (Y469 in rabbit), which has been shown to be important for ligand binding [13], is shifted toward the vanilloid pocket in the closed conformation and is shifted away in the open conformation (Fig. 5b). Comparing our fully open WT structure to our mutant structure, which both have open lower gates, we see very little differences in the position of S3 or the Y469 sidechain (Fig. 5c, d). Therefore, these changes in S3 appear to be dependent on the opening of the lower gate and independent of the upper gate conformation. How this movement of the S3 helix contributes to channel activity is unclear but given the proximity of the extracellular end of this helix to the pore turret (Fig. 3a), it's feasible that it may be a means of communication between the opening of the intracellular lower gate and the extracellular upper gate through a pore turret interaction.

The ankyrin repeat domains (ARD) are well resolved in both our WT and mutant structures and although high resolution crystal structures have been solved for this domain[42,43], it has been unclear how they participate in channel function. Aligning the ARDs of our fully open WT structure to the fully closed structure with respect to S1 and S2, we observe the whole domain shifting downward and away from where the plasma membrane would be (Fig. 5e) with a Cα RMSD of 4.27Å (Table 2). Conversely, the alignment of the WT and mutant structures reveals very little difference in position between the ARDs (Fig. 5f). It is unclear how ARDs contribute to TRP channel function but one hypothesis is that they act as springs capable of structurally storing and releasing energy[44–47].Perhaps the distinct ARD states we observe here represent a compressed and relaxed conformation coinciding with the open and closed states of the channel.

Structural analysis of the upper and lower gates

To understand the mechanism by which the upper and lower gates adopt these functionally distinct conformations with respect to the static S1 and S2 domains, we superimposed the WT TRPV2 models with those of our mutant structure and the fully closed TRPV2 structure (PDB: 5AN8) [17]. With these comparisons we observed and quantified significant differences

in the functionally important S5, S6, S4/S5 linker, TRP domain, pore loop, selectivity filter, and pore helix (Fig. 6).

In the fully open structure we see that the S6 helix, which lines the conduction pathway, tilts at a shallower angle with respect to the TRP segment as compared to the fully closed structure (Fig. 6a). At the intracellular end of S6, this change in tilt appears to be accommodated by a flexible S6/TRP “elbow” which transitions from a loop to a more helical secondary structure during channel opening. A similar transition at this “elbow” was also seen in the recent crystal structure of RTx-bound TRPV2 (Supplementary Fig. 7)[20]. As in the fully open state, the partially open mutant structure has a tilted S6 and a helical S6/TRP elbow (Fig. 6e, g), and in both open states the M645 sidechain, which blocks conduction at the lower gate in the fully closed structure,[17] is shifted away from the cation conduction pathway (Fig. 6c, g). However, the tilting of the mutant S6 helix appears to be more rigid than the WT S6, resulting in the extracellular end diverging from the open-state position by 2.2 Å as calculated by their Cα RMSDs (Fig. 6e,f, Supplementary Fig. 7b, and Table 2). Interestingly, the break in rigidity or bending in the WT S6 helix occurs at the position homologous to where a pi-helix is identified by comparison of TRPV2 and TRPV1 structures[13,17]. (Supplementary Fig. 7a, d). This S6 pi-helix was not present in the previously published fully closed TRPV2 structure (Fig. 6a and Supplementary Fig. 7c).[13,17] Therefore, the presence of this pi-helix may depend on the functional state of TRPV2 and/or the presence of the pore turret.

The position of the extracellular end of S6 and the presence of the pore turret appear to determine the open and closed states of the pore loop and selectivity filter (Fig. 6b, f). We observed large backbone and sidechain rearrangements within this area, with a calculated 3.36 Å Cα RMSD between the fully open WT and partially open mutant structures, and a 4.92 Å Cα RMSD between the WT and the fully closed structure (Table 2). Using the F612 side chain as an anchor point, we see that the backbone is differently arranged, pointing this residue’s sidechain towards the S5 helix in the mutant, whereas it is pointed away in both the WT structure and the fully closed structure (PDB:5AN8) (Fig. 6b, f). This configuration in our TRPV2 mutant is similar to the closed TRPV1 conformation at the homologous F649 residue (Supplementary Fig. 1e)[13]. As the TRPV1 constructs also had a pore turret deletion similar to our TRPV2 mutant which are both larger than the deletion made in the fully closed TRPV2 construct (PDB: 5AN8)[17], it is feasible that a pore turret of adequate length is necessary to compete for the space between the pore helix, pore loop and S5, thereby preventing the adoption of these possibly non-native closed states of the upper gate. Further supporting that the open state of the upper gate is sensitive to the arrangements of the pore loop is that minor mutagenic changes, substituting alanine for either L610 or F618, recapitulate the loss of 2-APB sensitivity for TRPV2 seen in our pore turret deletion mutant (Fig. 1b and Supplementary Fig. 1f).

Another dramatic difference between the fully open WT and fully closed structures at the upper gate is the shift of the pore helix position which is coupled to the movement of S5 (Fig. 6b, d). The resulting pore helix position is similar to what was observed in the RTx-bound TRPV2 crystal structure when aligned to the static S1 and S2 helices; however, the relative positions of S5 and S6 are dramatically different (Supplementary Fig. 1f). In our

open apo-structure of TRPV2, the extracellular end of S5 displaces the pore helix during channel opening, pushing it to its conductive position by both bending more steeply at its junction with the S4/S5 linker and by being pulled laterally by this same linker (Fig. 6d, c). Interestingly, the junction between the S5 helix and S4/S5 linker is another pi-helix site identified in the TRPV1 cryoEM structures, and more recently in the crystal structure of RTx-bound TRPV2, and appears to be a necessary pi-helix location in TRPV2 to accommodate these S5 movements[13–15,20,31]. The S4/S5 linker domain appears to be sliding laterally and perpendicularly over the regulatory TRP segment amounting to a ~5.4Å shift, or the distance of a whole helical turn, as demonstrated by using large sidechain residues as anchor points in the models (Fig. 6c). Importantly, this lateral movement perpendicular to the TRP region of the S5 helix and the S4/S5 linker do not occur in the ligand-dependent open states of the TRPV1 and TRPV2 structures (Supplementary Fig. 7d, e). However, the S4/S5 linker does appear to also move slightly outward similarly to what was previously described for TRPV1 and TRPV2, pulling with it the S6 helix and opening the lower gate (Fig. 6c and Supplementary Fig. 7d,e) [13–15,20,48]. Comparing the fully open TRPV2 structure to the pore-turret deletion mutant reveals that the registers of the lower end of S6 are different where the mutant adopts an intermediate position between the fully closed and fully open states. The mutant's inability to open fully at the lower gate (Fig. 6g, h). appears to be due to the absence of the S6 pi-helix which gives the added flexibility to achieve a fully open state as seen in both our WT TRPV2 structure and the previous TRPV1 structures. (Fig. 6c, g and Supplementary Fig. 7a, b) [13,14,20,31]

Discussion

The structures presented here to our knowledge include the first one for the TRPV family with a long and intact pore turret loop visible, and first ligand-free structures for TRPV2 or TRPV1 with an unoccupied vanilloid-binding site. At near-atomic resolutions, they exhibit distinct new conformations in the regions surrounding the ion permeation pathway, likely as consequences of these new structural features, and suggest a mechanism for the ligand-independent opening of TRPV2 (Fig. 7). An unanswered question is why the previously reported structure of TRPV2 with a pore turret deletion is in a fully closed state, whereas the mutant structure reported here, with a very similar deletion is in a partially open form, with an open lower gate. It would be somewhat surprising if minor differences in the details of the remaining pore turret sequences could exert such a large effect all the way from the extracellular surface to the lower gate. Alternatively, the presence or absence of a lipid or other ligand at the vanilloid binding site may be responsible for the difference in functional states.

Furthermore, the surprisingly planar structure of the pore turret and its arrangement parallel to the plasma membrane suggests that lipid interactions with the turret at the extracellular surface could play an important part in regulating channel activity; presumably those interactions would have to be polar in nature, given the lack of hydrophobic side chains in the turret. It will be interesting to observe interactions with lipids on both sides of the membranes by solving the full-length TRPV2 structure in reconstituted nano-discs. These could be used to test the hypotheses suggested by the current TRPV structures about the role

of phosphoinositides and whether they bind at the vanilloid binding pockets or in other locations.

The well-defined pore-turret represents the only extracellular structure of TRPV channels that presents a possible binding site for extracellular agonists, antagonists, or modulators. Whether any such regulatory interactions occur naturally is unknown, but the pore turret is a potential site for pharmacological targeting with ligands that do not have to be sufficiently hydrophobic to pass through the cell membrane, including designer antibodies.

The role of the pore turret has been the subject of some controversy. Our results are consistent with previous studies in that they confirm that the pore turret is not essential for TRPV channel assembly [13–15]; however, we demonstrate it does indeed exert a quantitative influence on channel activity (Fig. 1). This controversy likely arises because of the application of different kinds of measurements for channel activity employed in different studies. Previous electrophysiological experiments with TRPV1 constructs have found that substituting a poly-glycine chain of the same length for the turret eliminated the temperature sensing modality but did not significantly alter capsaicin activation [21–23]. Some groups have created large deletions in this domain and observed no effect on the temperature sensitivity or agonist activation[27], and yet others have observed that these same large deletions do affect both temperature and capsaicin sensitivity in a sodium-dependent manner [25]. Now we have found that shortening the pore turret beyond a critical length does significantly reduce TRPV sensitivity to agonists at physiological membrane potentials using a Ca^{2+}-flux assay (Fig. 1). The ability to observe the influence of the pore turret on channel properties may thus depend on how the channel is probed. One apparent discrepancy is that most experiments studying the activity of TRPVs in response to pore turret manipulations have been performed using the patch clamp method at high (+60 to +100 mV) positive holding potentials [14,15,21–23,27]. While TRP channels are not generally considered voltage-sensitive due to the relatively shallow dependence of conductance on voltage, with gating charges around 0.5e for TRPV1 at 25 °C [6,49], their activity is strongly voltage-dependent and there is little information on voltage-induced changes in structure. Furthermore, mutagenesis experiments in TRPV4 have also suggested that the voltage dependence mechanism operates in tandem with the intracellular gate [50]. Therefore, it is possible that recording channel activity at high positive potential instead of at physiological potentials may mask the influence of the pore turret on coupling the upper gate to the lower gate.

In summary, the cryo-EM structures of TRPV2 described here represent a substantial step forward in understanding the gating mechanisms of the polymodal TRPV channels. It is now clear that the pore turret is necessary to stabilize a fully open un-liganded channel by ensuring the proper rearrangements in the upper gate in response to the opening of the lower gate, which in turn, is regulated by intracellular stimuli such as lipid cofactors, and possibly other ligands binding to the ankyrin repeat domains or elsewhere. To understand more fully if the pore turret's control over the upper gate is due to direct or allosteric interactions with the pore loop domain and to determine if lipid interactions are involved, more structures corresponding to distinct physiological conditions will need to be solved.

Methods:

Liposome Assay

The defined lipids 1-palmitol-2-oleoyl-sn-glycerol-3-phosphoethanolamine, 1-palmitol-2-oleoyl-sn-glycerol-3-[phosphor-rac-(1-glycerol)], and 1-palmitol-2-oleoyl-sn-glycerol-3-phosphocholine (Avanti Polar Lipids) were solubilized in chloroform in a 3:1:1 molar ratio respectively totaling 1 mg. This blend of bulk lipids was then mixed with 1-heptadecanoyl-2-(5Z,8Z,11Z,14Z-eicosatetraenoyl)-sn-glycero-3-phospho-(1'-myo-inositol-4',5'-bisphosphate) (PIP_2) (Avanti Polar Lipids) as indicated at a 100:1 molar ratio respectively. The solvent was evaporated in glass vials using argon gas and then incubated overnight in a desiccator. Dried lipid-cakes were hydrated in 0.5 mL 25 mM HEPES pH 8, 150 mM NaCl, 100 μM or 50 μM Fluo-5N pentapotassium salt buffer and sonicated. Next, 100 μg of purified WT TRPV2 solubilized in 100 μM MNG was added to the lipid-dye mixture and incubated on a nutator for 1 h at 4C. The detergent was subsequently removed using 3, 2-hour rounds of incubation with 50 mg BioBeads (BioRad). Free Fluo-5N dye which was not trapped inside the resulting proteoliposomes was removed by running the solution through a 3.5 mL PD midiTrap G-25 column (GE Healthcare) equilibrated with a 25 mM HEPES pH 8, 150 mM NaCl buffer. Fractions were collected and tested for free Fluo-5N dye and only the fractions with dye trapped inside the proteoliposomes were used for the assay. Proteoliposome fractions with dye incorporation were loaded onto a 96-well plate and a time course of fluorescent signals (494/518) were measured using a FlexStation 3 (Molecular Devices) before and after the addition of 2 mM Ca^{2+}. Maximum responses for each proteoliposome sample were generated using 5 μM Ionomycin (Sigma) and were used for data normalization.

Cell-based activity assay

TRPV variants were cloned into a PcDNA3.1 expression vector and transfected into HEK cells on a 96 well plate using Lipofectamine 2000 (Invitrogen). 36 hours post-transfection, cells were washed with Krebs/Ringer/HEPES (KRH) buffer pH 7.4 containing 120 mM NaCl, 4.7 mM KCl, 2.2 mM $CaCl_2$, 10 mM HEPES, 1.2 mM KH_2PO_4, 1.2 mM $MgSO_4$, and 1.8 g/L glucose. The cells were then incubated for 1 h at 25 °C with 2.5 μM Fluo-4 AM (Invitrogen) fluorescent dye suspended in KRH buffer supplemented with 0.02% pluronic acid v/v and 1 mM probenecid to prevent dye efflux. After dye loading, extracellular dye was washed away with KRH buffer. Ca^{2+}-flux was then measured using a FlexStation3 (Molecular Devices) fluorescent plate reader in response to the respective agonists for each TRPV variant and a maximum fluorescent response was generated using 5 μM ionomycin (Sigma). Fluorescent response data were then processed by subtracting the baseline recordings and normalizing to the ionomycin response using the equation: $Response = (F - Fo) \div (Fmax - Fo)$. Reported dose response curves were produced using the maximum recorded response for each dose and normalizing to the maximum dose. Background responses were observed in the empty vector controls for 2-APB and GSK1016790. Therefore, these background signals were also processed using the same method and then subtracted from the respective TRPV2/4 data to generate the specific TRPV2/4 responses.

Cell-based PIP_2 modulation assay

HEK cells were co-transfected with 100 ng of each TRPV2, Lyn11-targeted FRB, and CF-Ins54p plasmids on a 96-well plate. Alternatively, empty PcDNA3.1 and CF-Inp(D281A) were substituted for TRPV2 and CF-Ins54p respectively for the appropriate controls. The transfected cells were incubated for 36 hours and prepared for the fluorescence Ca^{2+}-flux assay as described above. Using a FlexStation3 (Molecular Devices) baseline fluorescence was recorded for 30 seconds before addition of 5 μM rapamycin (Sigma) to rapidly reduce the PIP_2 levels in the inner leaflet of the plasma membrane. After a 1 min incubation, 100 μM 2-APB was added and then 5 μM ionomycin after another 1.5 minutes for data normalization. Activity data were then processed as described above to produce the reported normalized response traces.

Protein Purification

The first 32 residues of the YVC1 protein were fused to the N-termini of rTRPV2 (73 - 726) and rTRPV2 (73-726, Δ564-589) for enhanced expression and a 1D4 epitope tag was fused to the C-terminus for affinity purification. These constructs were cloned into a YepM plasmid and transfected into BJ5457 *S. cerevisiae* (ATCC) for constitutive heterologous expression. 5L cultures of yeast grown to an OD600 of 1.5 were pelleted and frozen in liquid nitrogen and stored at −80° C until freshly purified protein was needed. Yeast pellets were thawed on ice and then resuspended in 100 ml lysis buffer composed of 25 mM HEPES pH 8 and 300 mM sucrose. The cells were then lysed with a LM20 microfluidizer (Microfluidics) and membrane fractions were isolated with sequential centrifugation steps at 1000 g for 10 min, 10,000 g for 30 min, and 100,000 g for 2 hr. Isolated membranes were then immediately homogenized in solubilization buffer without detergent (25 mM HEPES pH 8, 300 mM NaCl, 2 mM DTT, 10 % glycerol) with a glass homogenizer and then incubated with complete solubilization buffer (25 mM HEPES pH 8, 300 mM NaCl, 2 mM DTT, 10 % glycerol, and 5 mM lauryl maltose neopentyl glycol (MNG) (Anatrace)) at 4° C for 30 min. After detergent solubilization, samples were centrifuged again at 100,000 g for 1 h and the remaining soluble fraction was applied to a 3 ml 1D4 affinity column at 4° C. The 1D4 column was then washed with 10 column volumes of wash buffer composed of 25 mM HEPES pH 8, 300 mM NaCl, 2 mM DTT, 10% glycerol, and 0.5 mM MNG. TRPV2 was eluted from the column by incubating the column overnight with 3 ml 10 mg/ml 1D4 peptide solubilized in wash buffer. The eluted protein was then concentrated to 0.5 ml and then further purified by size exclusion chromatography using a 20 ml Superdex 200 SEC column (GE Healthcare) with the running buffer containing 25 mM HEPES pH 8, 300 mM NaCl, 2 mM DTT and 50 μM MNG.

Specimen preparation and Cryo-EM data acquisition.

Vitrified specimens of the purified protein were prepared by plunge-freezing on Quantifoil holey grids (Quantifoil Micro Tools GmbH) covered with a freshly prepared thin continuous carbon film. For the WT construct, images of frozen-hydrated sample particles were acquired on a Technai G2 Polara electron microscope (FEI) operated at 300 kV using a K2 Summit direct electron detector camera (Gatan). For the mutant construct we used a 300 kV JEM3200FSC (JEOL) with an in-column energy filter (20 eV), which increases particle

contrast. Movie stacks were collected in dose fractionation super-resolution counting mode at a nominal magnification of 415,000x (WT) and 425,100x (mutant) on each microscope, corresponding to calibrated physical pixel sizes of 1.26 Å and 1.23 Å, and super-resolution pixel sizes of 0.63 Å and 0.615 Å. The dose rate on the cameras was set to 10 electrons pixel $^{-1}$s $^{-1}$. The total exposure time was 10 s, leading to a total accumulated dose of 63 electrons Å^{-2} on the specimen. Each image stack was fractionated into 50 sub-frames, each with an accumulation time of 0.2 s per frame. Images were acquired at the defocus range of −1 to −3.5 μm (WT) and −0.7 to −3 μm (mutant) (Table 1).

Image processing and 3D reconstruction.

Dose-fractionated super-resolution raw image stacks of ice-embedded TRPV2 were binned 2 × 2 by Fourier cropping resulting in a pixel size of 1.26 Å (WT) and 1.23 Å (mutant) for further image processing. Each image stack was subjected to motion correction using 'dosefgpu_driftcorr'[51], and a sum of subframes 2-50 in each image stack was used for further image processing. We used 'e2evalimage.py' in the EMAN 2.1 package to select 1,921 micrographs from a total of 2,164 micrographs (WT) and 1,669 from 2,125 (mutant) micrographs for subsequent processing. The signal in the motion-corrected images extends beyond 4 Å (Supplementary Fig. 4b). For single particle reconstruction, 494,689 (WT) and 160,100 particles (mutant) were boxed out manually using 'e2boxer.py'. Image processing was then performed independently in both RELION1.4 and EMAN 2 beginning with the same set of boxed out particles. For the RELION1.4 reconstructions, defocus and astigmatism were determined for each micrograph by CTFFIND3 [52]. 2D averages of TRPV2 were first generated by EMAN2 then used to generate initial models with C4 symmetry imposed. These initial models were low-pass filtered to 60 Å resolution and used as a starting model for the RELION refinements. After this step, we ran several rounds of iterative 3D classification and 3D auto refinement to extract 11,789 particles (WT) and 50,509 particles (mutant) as the most self-consistent subset of the particle data set for the further analysis. Next, we generated a sum of sub-frames 2 to 16 frames of the same dataset and used them for the final refinement. We used gold standard procedures for both dataset refinements [53–55] . The Fourier shell correlation (FSC) 0.143 cut-off was used to estimate the resolution of final 3D reconstructions with a soft auto-mask in RELION post-processing (Supplementary Fig. 4b, and 4e). FSC curves were also calculated for the model vs the half maps and the whole maps (Supplementary Fig. 4g and 4h). RELION1.4 density map was sharpened by applying a B-factor of −95 Å^2 (WT) and −99 Å^2 (mutant) that was estimated by an automated procedure using the Bfactor program from the Grigorieff lab and visualized with Chimera [56] (Table 1, Supplementary Fig. 6). EMAN2.1 maps were automatically filtered as part of the refinement. Local resolution variations were estimated using ResMap [57] with two independent density maps without applying a mask (Supplementary Fig. 4a and 4d).

Modeling and model optimization

Cryo-EM density maps were first scaled to the crystal structure of the TRPV2 ankyrin repeat domain (PDB: 2ETB). Atomic models were then built in COOT [58] starting with the rabbit TRPV2 structure (PDB: 5AN8) as a homology model and then modified manually. The pore turret backbone was built *de novo* placing the prolines at the sharp turns observed in the

density. Model refinement was then performed using PHENIX [59] Real Space Refinement with secondary structure and geometry restraints. Simulated annealing was used in the first round of model optimization, and in the subsequent rounds only global minimization and atomic displacement parameters were used to reach converged models. Overfitting was monitored by producing even and odd maps with the gold-standard refinement approach, optimizing the model using the even map, and then testing it against the odd map. Average atomic displacement parameters (also known as B-factors) for each residue were calculated using methods described previously [60] to quantitatively annotate the models at different regions (Supplementary Fig. 6). EMRinger was then run, producing scores of 1.20 for the WT model and 1.31 for the mutant model, which are higher than the average scores of previously reported models of cryo-EM maps at similar resolutions [61].

QUANTIFICATION AND STATISTICAL ANALYSIS

GraphPad Prism was used to calculate the dose response curves for the TRPV channel activities. Quantitative evaluation and statistical analysis of the cryo-EM maps and models were as described above.

Reporting Summary

Further information on experimental design is available in the Nature Research Reporting Summary linked to this article.

Data availability

The rat TRPV2 models (PDB 6BO4, WT and PDB 6BO5, Mutant) and cryo-EM density maps (EMD-7118, WT and EMD-7119, Mutant) have been deposited in the protein data bank (http://www.rcsb.org) and the Electron Microscopy Data Bank (https://www.ebi.ac.uk/pdbe/emdb/. Other data are available from the corresponding authors upon reasonable request.

Supplementary Material

Refer to Web version on PubMed Central for supplementary material.

Acknowledgments:

We thank Dr. Corey Hryc for providing his expertise in modeling cryo-EM density maps and helping to validate the models. We thank Melina Agosto, Jennifer Gonzalez, and other members of the Wensel lab for helpful discussions and suggestions and Professor Ming Zhou for helpful comments. We thank the National Center for Macromolecular Imaging for providing the cryo-EM and computational resources. This work was supported by the Robert Welch Foundation (Q0035 and Q-1967-20180324) and a training fellowship from the Keck Center of the Gulf Coast Consortia, of the Houston Area Molecular Biophysics Program, National Institute of General Medical Sciences, T32GM008280. Further support was provided by the National Institutes of Health grants (P41GM103832, R01GM072804, R01EY007981, R01EY026545), and the American Heart Association (16GRNT29720001).

References

1. Clapham DE TRP channels as cellular sensors. Nature 426, 517–24 (2003). [PubMed: 14654832]
2. Clapham DE, Runnels LW & Strubing C The TRP ion channel family. Nat Rev Neurosci 2, 387–96 (2001). [PubMed: 11389472]

3. Montell C et al. A unified nomenclature for the superfamily of TRP cation channels. Mol Cell 9, 229–31 (2002). [PubMed: 11864597]
4. Jordt SE & Ehrlich BE TRP channels in disease. Subcell Biochem 45, 253–71 (2007). [PubMed: 18193640]
5. Nilius B TRP channels in disease. Biochim Biophys Acta 1772, 805–12 (2007). [PubMed: 17368864]
6. Nilius B et al. Gating of TRP channels: a voltage connection? J Physiol 567, 35–44 (2005). [PubMed: 15878939]
7. Li M, Yu Y & Yang J Structural biology of TRP channels. Adv Exp Med Biol 704, 1–23 (2011). [PubMed: 21290287]
8. Kaneko Y & Szallasi A Transient receptor potential (TRP) channels: a clinical perspective. Br J Pharmacol 171, 2474–507 (2014). [PubMed: 24102319]
9. Wong GY & Gavva NR Therapeutic potential of vanilloid receptor TRPV1 agonists and antagonists as analgesics: Recent advances and setbacks. Brain Res Rev 60, 267–77 (2009). [PubMed: 19150372]
10. Carnevale V & Rohacs T TRPV1: A Target for Rational Drug Design. Pharmaceuticals (Basel) 9(2016).
11. Reilly RM et al. Pharmacology of modality-specific transient receptor potential vanilloid-1 antagonists that do not alter body temperature. J Pharmacol Exp Ther 342, 416–28 (2012). [PubMed: 22570364]
12. Brown W et al. Safety, Pharmacokinetics, and Pharmacodynamics Study in Healthy Subjects of Oral NEO6860, a Modality Selective Transient Receptor Potential Vanilloid Subtype 1 Antagonist. J Pain 18, 726–738 (2017). [PubMed: 28188907]
13. Gao Y, Cao E, Julius D & Cheng Y TRPV1 structures in nanodiscs reveal mechanisms of ligand and lipid action. Nature 534, 347–51 (2016). [PubMed: 27281200]
14. Cao E, Liao M, Cheng Y & Julius D TRPV1 structures in distinct conformations reveal activation mechanisms. Nature 504, 113–8 (2013). [PubMed: 24305161]
15. Liao M, Cao E, Julius D & Cheng Y Structure of the TRPV1 ion channel determined by electron cryo-microscopy. Nature 504, 107–12 (2013). [PubMed: 24305160]
16. Huynh KW et al. Structure of the full-length TRPV2 channel by cryo-EM. Nat Commun 7, 11130 (2016). [PubMed: 27021073]
17. Zubcevic L et al. Cryo-electron microscopy structure of the TRPV2 ion channel. Nat Struct Mol Biol 23, 180–186 (2016). [PubMed: 26779611]
18. Saotome K, Singh AK, Yelshanskaya MV & Sobolevsky AI Crystal structure of the epithelial calcium channel TRPV6. Nature 534, 506–11 (2016). [PubMed: 27296226]
19. Yin Y et al. Structure of the cold- and menthol-sensing ion channel TRPM8. Science 359, 237–241 (2018). [PubMed: 29217583]
20. Zubcevic L, Le S, Yang H & Lee SY Conformational plasticity in the selectivity filter of the TRPV2 ion channel. Nat Struct Mol Biol 25, 405–415 (2018). [PubMed: 29728656]
21. Yang F, Cui Y, Wang K & Zheng J Thermosensitive TRP channel pore turret is part of the temperature activation pathway. Proc Natl Acad Sci U S A 107, 7083–8 (2010). [PubMed: 20351268]
22. Cui Y et al. Selective disruption of high sensitivity heat activation but not capsaicin activation of TRPV1 channels by pore turret mutations. J Gen Physiol 139, 273–83 (2012). [PubMed: 22412190]
23. Yang F, Ma L, Cao X, Wang K & Zheng J Divalent cations activate TRPV1 through promoting conformational change of the extracellular region. J Gen Physiol 143, 91–103 (2014). [PubMed: 24344245]
24. Winter Z et al. Functionally important amino acid residues in the transient receptor potential vanilloid 1 (TRPV1) ion channel--an overview of the current mutational data. Mol Pain 9, 30 (2013). [PubMed: 23800232]
25. Jara-Oseguera A, Bae C & Swartz KJ An external sodium ion binding site controls allosteric gating in TRPV1 channels. Elife 5(2016).

26. Jordt SE, Tominaga M & Julius D Acid potentiation of the capsaicin receptor determined by a key extracellular site. Proc Natl Acad Sci U S A 97, 8134–9 (2000). [PubMed: 10859346]
27. Ryu S, Liu B, Yao J, Fu Q & Qin F Uncoupling proton activation of vanilloid receptor TRPV1. J Neurosci 27, 12797–807 (2007). [PubMed: 18032651]
28. Munns CH, Chung MK, Sanchez YE, Amzel LM & Caterina MJ Role of the outer pore domain in transient receptor potential vanilloid 1 dynamic permeability to large cations. J Biol Chem 290, 5707–24 (2015). [PubMed: 25568328]
29. Yang F, Vu S, Yarov-Yarovoy V & Zheng J Rational design and validation of a vanilloid-sensitive TRPV2 ion channel. Proc Natl Acad Sci U S A 113, E3657–66 (2016). [PubMed: 27298359]
30. Zhang F et al. Engineering vanilloid-sensitivity into the rat TRPV2 channel. Elife 5(2016).
31. Cao E, Cordero-Morales JF, Liu B, Qin F & Julius D TRPV1 channels are intrinsically heat sensitive and negatively regulated by phosphoinositide lipids. Neuron 77, 667–79 (2013). [PubMed: 23439120]
32. Doerner JF, Hatt H & Ramsey IS Voltage- and temperature-dependent activation of TRPV3 channels is potentiated by receptor-mediated PI(4,5)P2 hydrolysis. J Gen Physiol 137, 271–88 (2011). [PubMed: 21321070]
33. Mercado J, Gordon-Shaag A, Zagotta WN & Gordon SE Ca2+-dependent desensitization of TRPV2 channels is mediated by hydrolysis of phosphatidylinositol 4,5-bisphosphate. J Neurosci 30, 13338–47 (2010). [PubMed: 20926660]
34. Lukacs V et al. Dual regulation of TRPV1 by phosphoinositides. J Neurosci 27, 7070–80 (2007). [PubMed: 17596456]
35. Rohacs T Phosphoinositide regulation of TRPV1 revisited. Pflugers Arch 467, 1851–69 (2015). [PubMed: 25754030]
36. Ufret-Vincenty CA et al. Mechanism for phosphoinositide selectivity and activation of TRPV1 ion channels. J Gen Physiol 145, 431–42 (2015). [PubMed: 25918361]
37. Suh BC, Inoue T, Meyer T & Hille B Rapid chemically induced changes of PtdIns(4,5)P2 gate KCNQ ion channels. Science 314, 1454–7 (2006). [PubMed: 16990515]
38. Klein RM, Ufret-Vincenty CA, Hua L & Gordon SE Determinants of molecular specificity in phosphoinositide regulation. Phosphatidylinositol (4,5)-bisphosphate (PI(4,5)P2) is the endogenous lipid regulating TRPV1. J Biol Chem 283, 26208–16 (2008). [PubMed: 18574245]
39. Ramachandran GN, Ramakrishnan C & Sasisekharan V Stereochemistry of polypeptide chain configurations. J Mol Biol 7, 95–9 (1963). [PubMed: 13990617]
40. Smart OS, Neduvelil JG, Wang X, Wallace BA & Sansom MS HOLE: a program for the analysis of the pore dimensions of ion channel structural models. J Mol Graph 14, 354–60, 376 (1996). [PubMed: 9195488]
41. Matta JA & Ahern GP Voltage is a partial activator of rat thermosensitive TRP channels. J Physiol 585, 469–82 (2007). [PubMed: 17932142]
42. Jin X, Touhey J & Gaudet R Structure of the N-terminal ankyrin repeat domain of the TRPV2 ion channel. J Biol Chem 281, 25006–10 (2006). [PubMed: 16809337]
43. McCleverty CJ, Koesema E, Patapoutian A, Lesley SA & Kreusch A Crystal structure of the human TRPV2 channel ankyrin repeat domain. Protein Sci 15, 2201–6 (2006). [PubMed: 16882997]
44. Sotomayor M, Corey DP & Schulten K In search of the hair-cell gating spring elastic properties of ankyrin and cadherin repeats. Structure 13, 669–82 (2005). [PubMed: 15837205]
45. Lee G et al. Nanospring behaviour of ankyrin repeats. Nature 440, 246–9 (2006). [PubMed: 16415852]
46. Gaudet R A primer on ankyrin repeat function in TRP channels and beyond. Mol Biosyst 4, 372–9 (2008). [PubMed: 18414734]
47. Corey DP & Sotomayor M Hearing: tightrope act. Nature 428, 901–3 (2004). [PubMed: 15118709]
48. Gavva NR et al. Molecular determinants of vanilloid sensitivity in TRPV1. J Biol Chem 279, 20283–95 (2004). [PubMed: 14996838]
49. Voets T et al. The principle of temperature-dependent gating in cold- and heat-sensitive TRP channels. Nature 430, 748–54 (2004). [PubMed: 15306801]

50. Loukin S, Su Z, Zhou X & Kung C Forward genetic analysis reveals multiple gating mechanisms of TRPV4. J Biol Chem 285, 19884–90 (2010). [PubMed: 20424166]

Methods-only references

51. Li X et al. Electron counting and beam-induced motion correction enable near-atomic-resolution single-particle cryo-EM. Nat Methods 10, 584–90 (2013). [PubMed: 23644547]
52. Mindell JA & Grigorieff N Accurate determination of local defocus and specimen tilt in electron microscopy. J Struct Biol 142, 334–47 (2003). [PubMed: 12781660]
53. Henderson R et al. Outcome of the first electron microscopy validation task force meeting. Structure 20, 205–14 (2012). [PubMed: 22325770]
54. Scheres SH & Chen S Prevention of overfitting in cryo-EM structure determination. Nat Methods 9, 853–4 (2012). [PubMed: 22842542]
55. Scheres SH RELION: implementation of a Bayesian approach to cryo-EM structure determination. J Struct Biol 180, 519–30 (2012). [PubMed: 23000701]
56. Pettersen EF et al. UCSF Chimera--a visualization system for exploratory research and analysis. J Comput Chem 25, 1605–12 (2004). [PubMed: 15264254]
57. Kucukelbir A, Sigworth FJ & Tagare HD Quantifying the local resolution of cryo-EM density maps. Nat. Methods 11, 63–65 (2014). [PubMed: 24213166]
58. Emsley P, Lohkamp B, Scott WG & Cowtan K Features and development of Coot. Acta Crystallogr D Biol Crystallogr 66, 486–501 (2010). [PubMed: 20383002]
59. Adams PD et al. PHENIX: a comprehensive Python-based system for macromolecular structure solution. Acta Crystallogr D Biol Crystallogr 66, 213–21 (2010). [PubMed: 20124702]
60. Hryc CF et al. Accurate model annotation of a near-atomic resolution cryo-EM map. Proc Natl Acad Sci U S A 114, 3103–3108 (2017). [PubMed: 28270620]
61. Barad BA et al. EMRinger: side chain-directed model and map validation for 3D cryo-electron microscopy. Nat Methods 12, 943–6 (2015). [PubMed: 26280328]

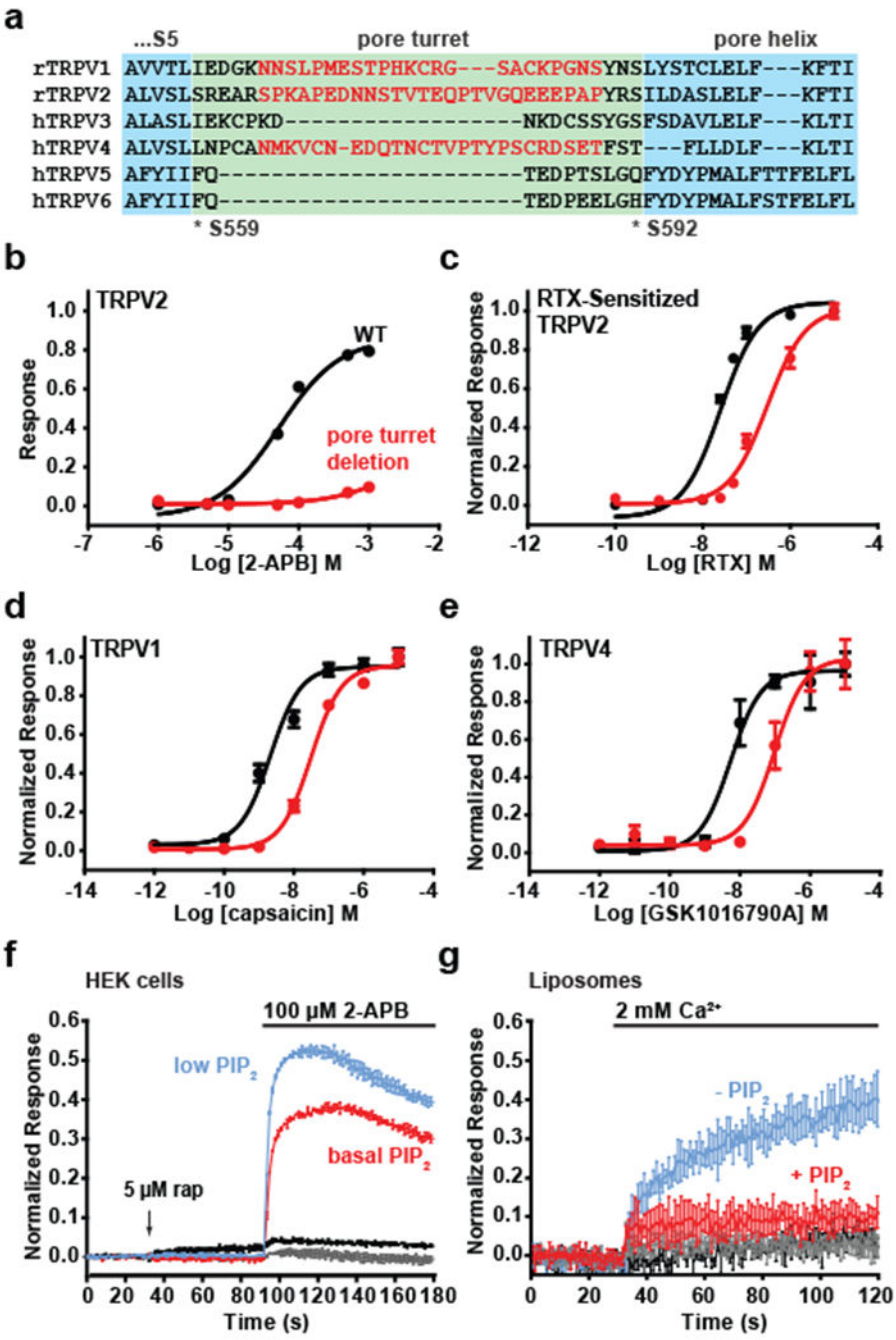

Fig. 1|.

Effects of pore turret deletions and phosphoinositides on channel activity.

(A) Sequence alignment of the pore turret domains of the TRPV family. Red sequences indicate the deleted regions in the constructs referred to in (B), (C), (D), and (E). Asterisks indicate the first and last residues of the rat TRPV2 pore turret. (B)(D)(E) Dose responses of TRPVs comparing the activities of full-length and pore-turret-deletion variants. Data points are represented as mean ± SEM (n = 3 technical repeats). (C) Dose response for full-length TRPV2 with four amino acid substitutions (F472S, L503F, L510T, Q530E) which confer

sensitivity to resiniferatoxin (RTX) and for a pore turret deletion variant with the same substitutions. Data points are represented as mean ± SEM (n = 3 technical repeats). (F) Normalized fluorescent traces for a cell-based Ca2+-flux activity assay demonstrating the potentiation effect of activating a PIP2 phosphatase on TRPV2 activity. Data points are represented as mean ± SEM (n = 3 technical repeats). Empty vector control responses in the precence of low PIP2 levels is indicated by the blackline and the grey line indicates the response with PIP2 at basal levels. (G) Normalized fluorescent traces for a liposome-based Ca2+-flux assay demonstrating the activity of reconstituted full-length TRPV2 and the inhibitory effect of PIP2. Data points are represented as mean ± SEM (n = 3, technical repeats). Empty liposomes responses in the presence of PIP2 is indicated by the grey line and in the absence of PIP2 is indicated by the black line.

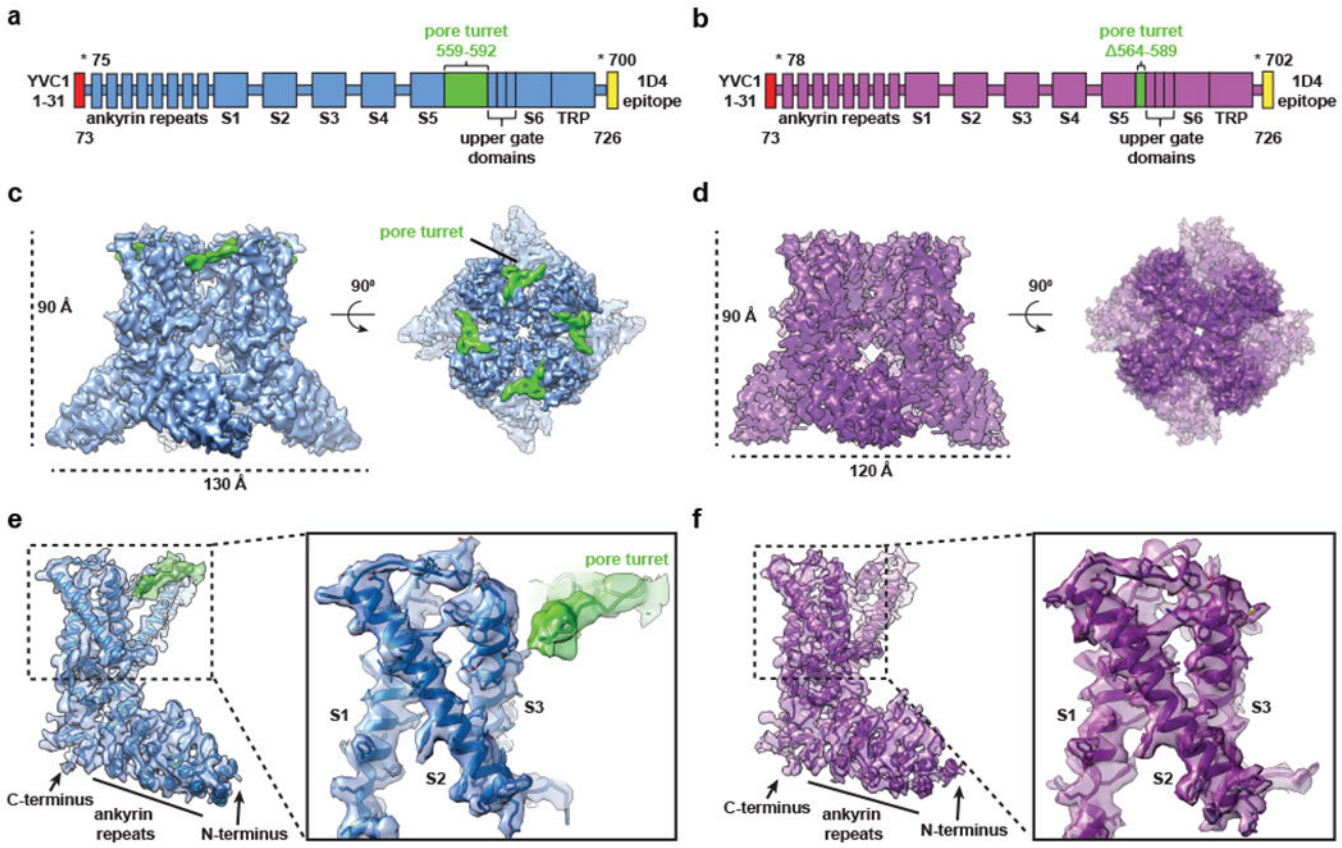

Figure 2|.

TRPV2 Constructs and cryo-EM Density Maps

(A) (B) WT (blue) and mutant (purple) constructs of TRPV2 used for biochemical characterization and structural determination. Both contain the rat TRPV2 sequence spanning residues 73 to 726; however, the mutant construct has a deletion in the pore turret loop from residues 564 to 589. The coverage of the cryo-EM density maps are in between the residue numbers with an asterisk. (C) Cryo-EM density map for full-length TRPV2 tetramer (blue) with the pore turret (green) visible. (D) Density map for mutant TRPV2 tetramer (purple) showing the missing density in the pore turret region. (E)(F) Models for the WT and mutant TRPV2 monomers fit to segmented maps, and a zoom view showing S1, S2, and S3 helices to display sidechain features.

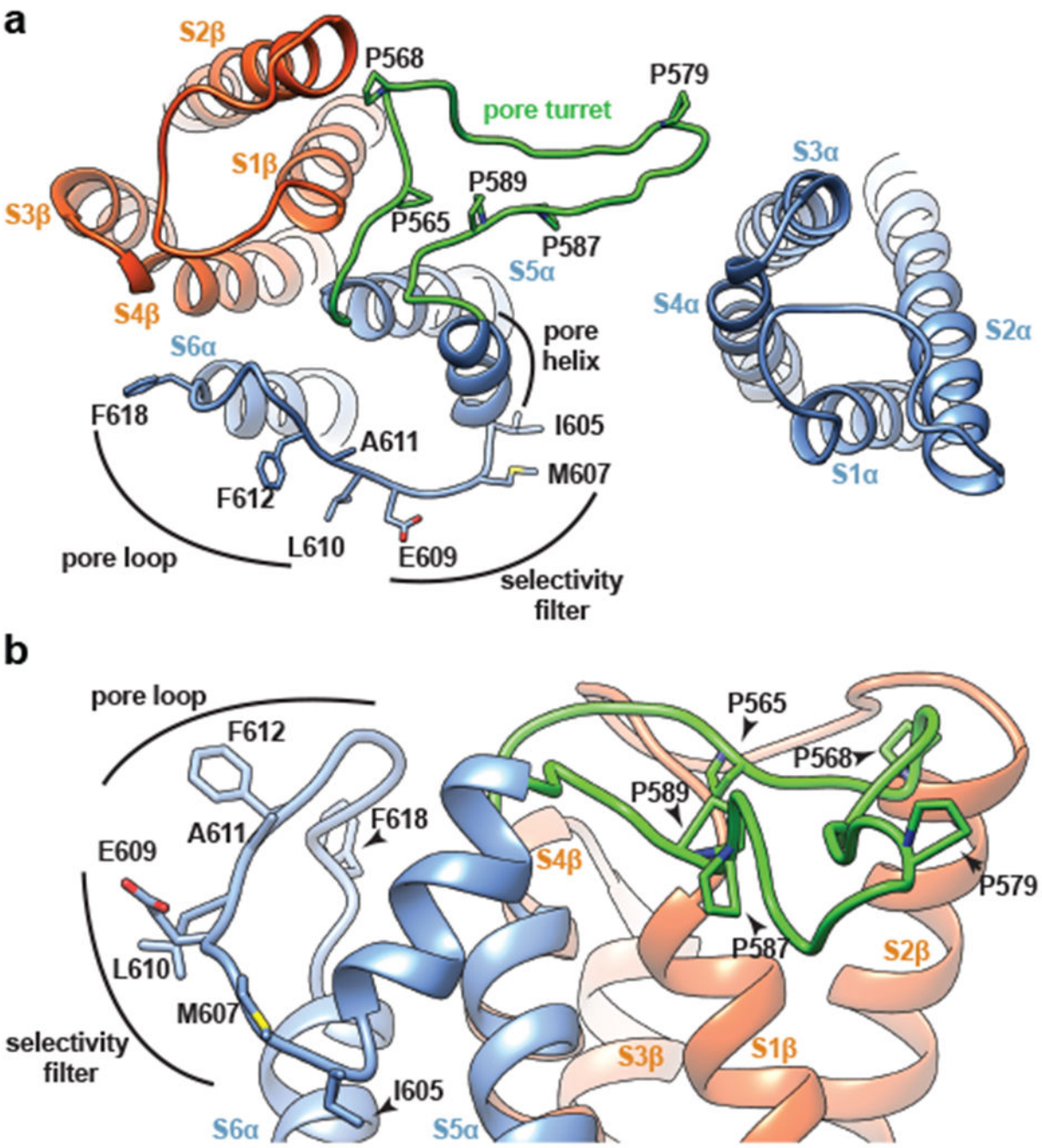

Fig. 3|.

Structure and Orientation of Pore Turret Domain

(A) The arrangment of the pore turret (green) with respect to the upper gating domains and transmembrane domains of its own subunit (blue) and the transmembrane domains of the adjacent subunit (orange). (B) Side view of the pore turret domain showing its planar structure and perpendicular orientation to the transmembrane domains.

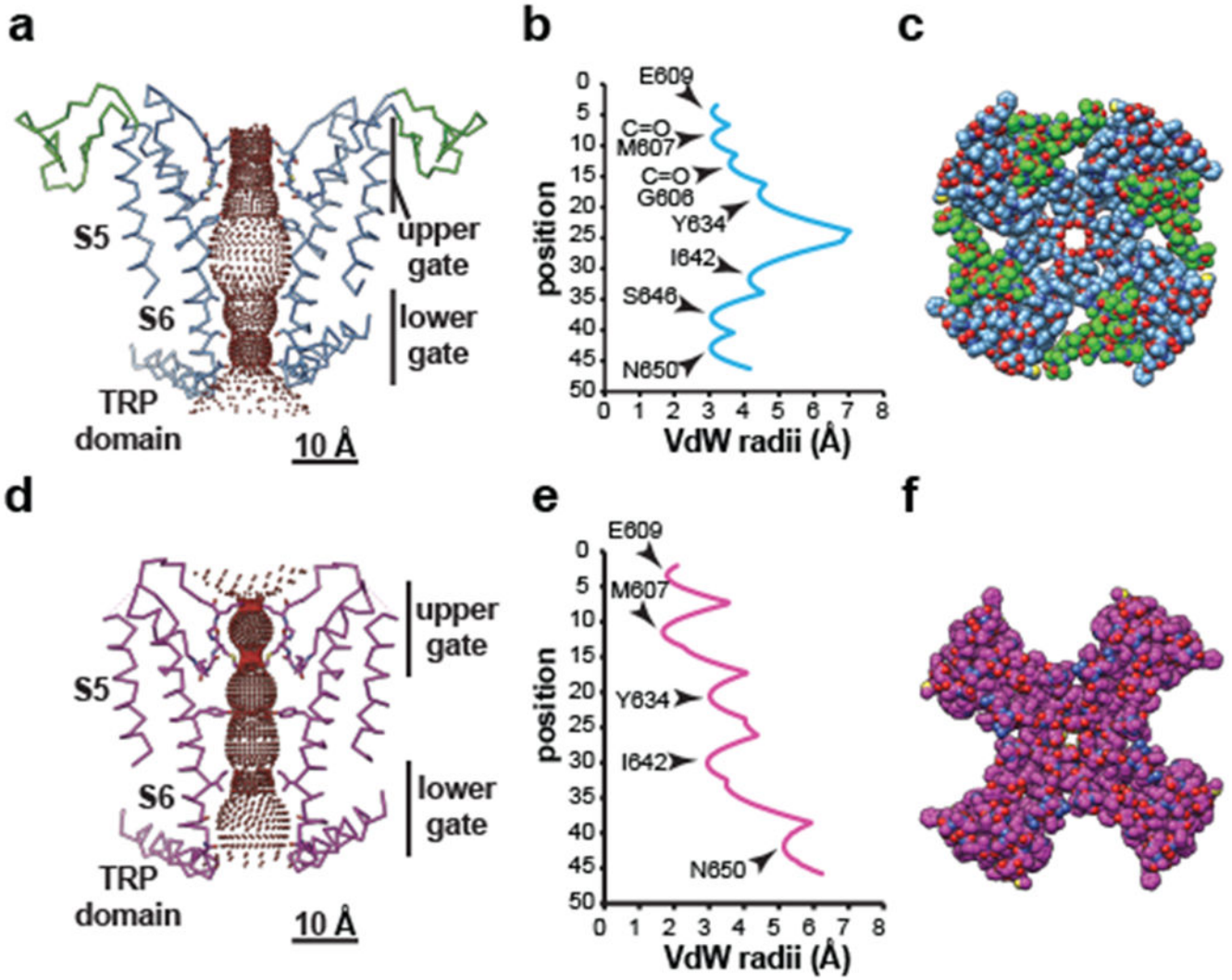

Fig. 4|.

Cation Pathway of WT and Mutant Variants of TRPV2.

(A)(D) S5 and S6 transmembrane segments of the two TRPV2 variants and dot surfaces of the conduction pathways. Black lines indicate the upper and lower gating regions. (B)(E) Van der Vaals radii along the conduction pathway with positions of important residues indicated with arrows and labels. (C)(F) Space filling representation of the WT and Mutant pores looking down through the extracellular side of the channel. Blue, nitrogen; red, oxygen; green, carbons in pore turret; cyan, carbon in rest of WT model; magenta, carbon in mutant model.

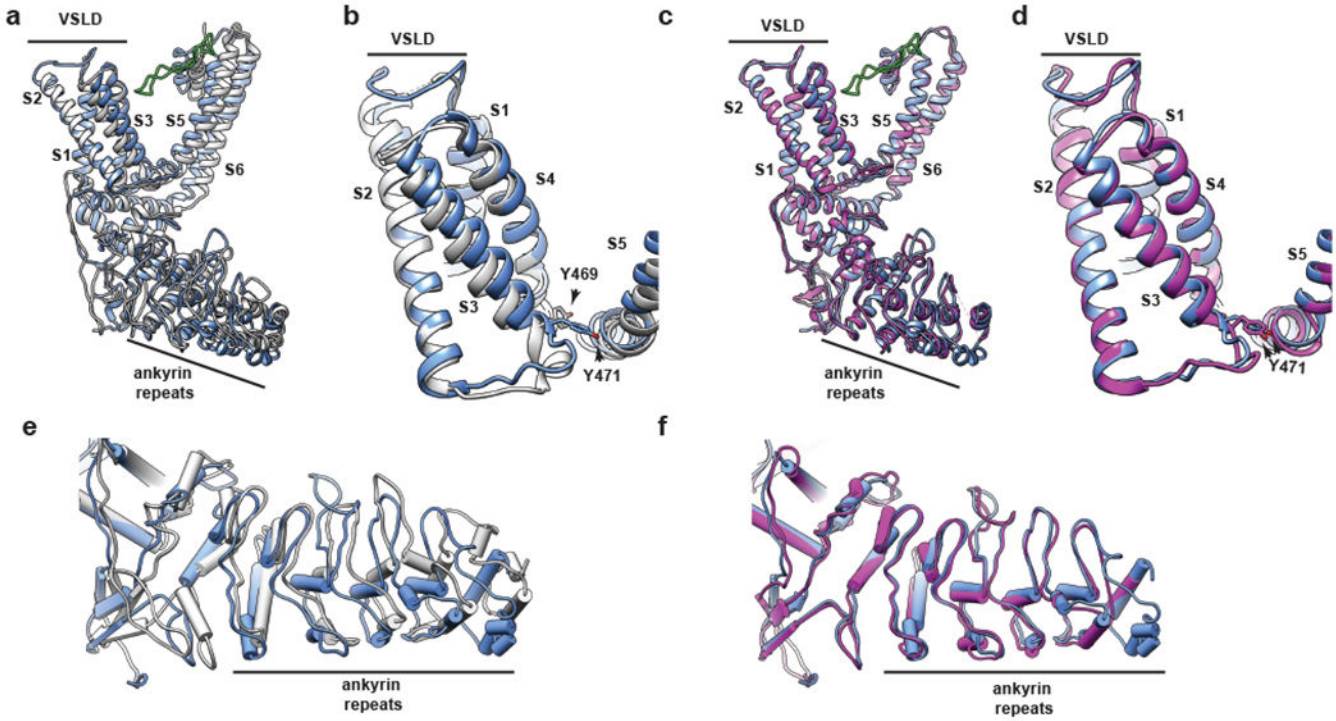

Fig. 5|.

Comparisons of TRPV2 structures.

Cyan, WT; grey, (A, B, E), fully-closed (PDB: 5AN8); magenta, (C, D, F), Mutant. (A, C) full model alignments based on S1 and S2 positions. (B, D) Voltage-sensing-like domain (VSLD) region showing a shift in the S3 position between the open and closed structures. (E, F) Alignment of Pipes and planksrepresentations of the ankyrin repeat domains.

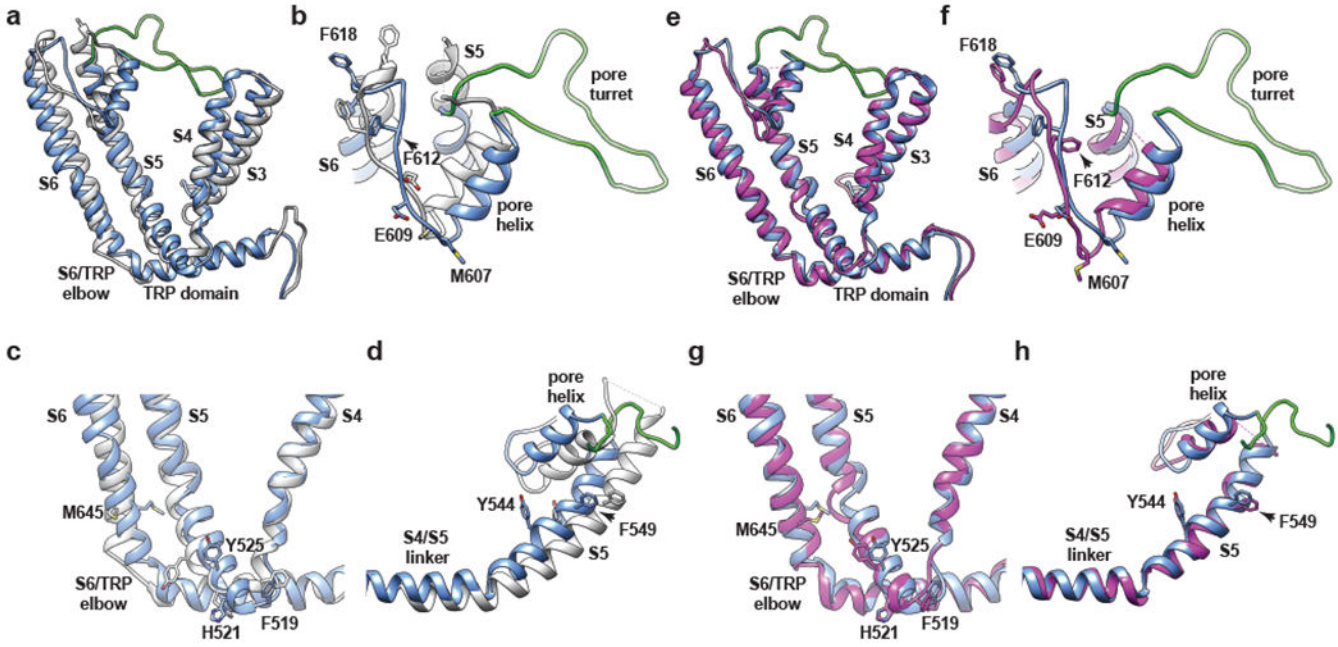

Fig. 6|.

Model alignments of S3-S6.

Alignments are based on S1 and S2 as in Fig. 5.(A)(E) Alignments of S3-S6 of fully closed TRPV2 sructure (grey) (5AN8) and partially open mutant TRPV2 (purple) with the fully-open WT TRPV2 structure (blue) (B)(F) Alignments of the upper gate including the pore helix, selectivity filter, pore loop, and upper S6 regions. (C) (G) View of the aligned S4/S5 linker domains and their relative positions to S6 and the TRP domain. (D) (H) Relative positions of the S5 and pore helices.

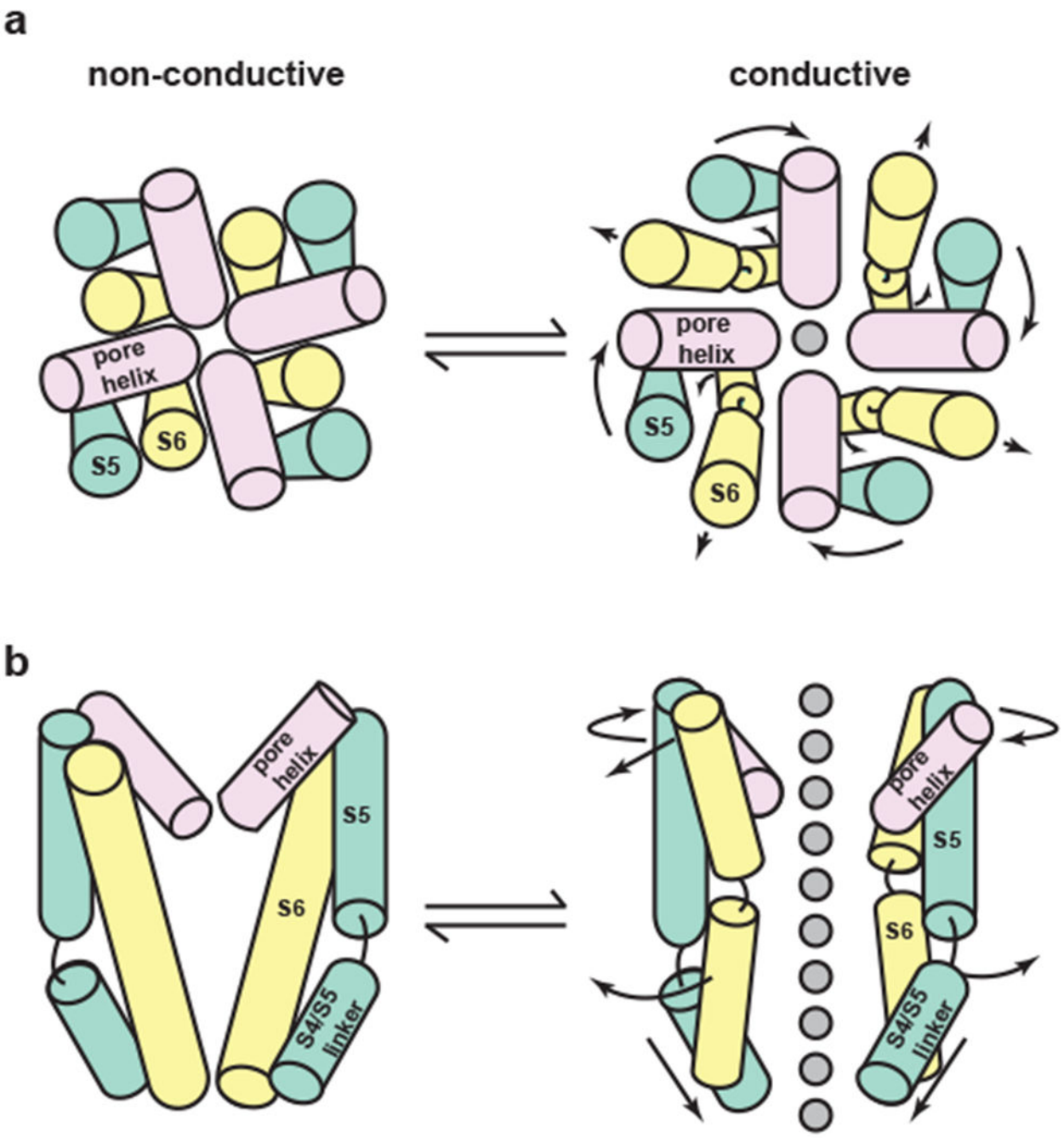

Figure 7|.

Model Mechanism for agonist-independent TRPV2 activation.

(A) Top view of the TRPV2 tetramer looking down the cation pathway from the extracellular side. (B) Sideview for a crossection of TRPV2 displaying two apposing subunits.

Table 1.

Cryo-EM data collection, refinement and validation statistics

	#1 name (EMD-7118, PDB 6BO4)	#2 name (EMD-7119, PDB 6BO5)
Data collection and processing		
Magnification	415,000	425,100
Voltage (kV)	300	300
Electron exposure (e^{-}/Å^2)	63 over 50 frames; 2-16 used for refinement	63 over 50; 2-16 used for refinement
Defocus range (μm)	1-3.5	0.7-3.0
Pixel size (Å)	1.26	1.23
Symmetry imposed	C4	C4
Initial particle images (no.)	494,689	160,100
Final particle images (no.)	11,789	50,509
Map resolution (Å)	4.0	3.6
FSC threshold	0.143	0.143
Map resolution range (Å)	3.5-5.5	3.5-5.5
Refinement		
Initial model used (PDB code)	2ETB & 5AN8	2ETB & 5AN8
Model resolution (Å)	4	3.6
FSC threshold	.143	.143
Model resolution range (Å)	3.5-5.5	3.5-5.5
Map sharpening *B* factor (Å^2)	−95	−99
Model composition		
Nonhydrogen atoms	18,432	17,236
Protein residues	2,500	2,228
Ligands	0	0
B factors (Å^2)		
Protein	−95	−99
Ligand	n.a.	n.a.
R.m.s. deviations		
Bond lengths (Å)	.008	.005
Bond angles (°)	1.532	1.295
Validation		
MolProbity score	2.26	2.32
Clashscore	16.39	11.58
Poor rotamers (%)	.75	1.84
Ramachandran plot		
Favored (%)	90.34	90.48
Allowed (%)	9.5	9.16
Disallowed (%)	.16	.36

Table 2.

Key Structural Differences Between Functional States

Domain and residue range	WT/Mutant RMSD Cα (Å)	WT/5AN8 RMSD Cα (Å)
Selectivity filter/pore loop (G606-R619)	3.34	4.96
Pore Helix (A595-I605)	2.02	5.27
S6 (G620-L638)	2.20	4.72
S6/TRP elbow (V635-A653)	2.32	5.23
S5 (D536-S557)	1.31	5.28
S4/S5 linker (F519-R535)	1.19	5.45
TRP Domain (D654-G674)	1.14	2.02
S3 (Y471-M492)	0.75	3.12
Ankyrin Repeats (R175-E185)	1.16	4.27